Received 2 May 2023; revised 20 June 2023; accepted 3 July 2023. Date of publication 11 July 2023; date of current version 31 July 2023.

Digital Object Identifier 10.1109/OJAP.2023.3294244

Tuning the Angular Characteristics of Biomimetic Antenna Arrays

INES DORSCH (Graduate Student Member, IEEE), DOMINIK SCHWARZ (Graduate Student Member, IEEE), SARAH FORSTER, AND CHRISTIAN WALDSCHMIDT (Fellow, IEEE)

Institute of Microwave Engineering, Ulm University, 89081 Ulm, Germany

CORRESPONDING AUTHOR: I. DORSCH (e-mail: ines.dorsch@uni-ulm.de)

This work was supported by the German Research Foundation (DFG, Deutsche Forschungsgemeinschaft) under Grant WA 3506/6-2.

ABSTRACT The angle estimation capabilities of radar sensors are strictly linked to the antenna spacing between the array elements. A larger array aperture corresponds to a smaller beam width or in terms of the angle estimation a higher phase sensitivity. So-called Biomimetic Antenna Arrays (BMAAs) provide the opportunity to shape the angular characteristics with more degrees of freedom. In this work, the concept and the design process of a tunable BMAA are presented. By electronically tuning varactor diodes, such an array can adapt its angular characteristics depending on the direction-of-arrival (DoA) and signal strength of a radar target. The theoretical requirements for the desired task are examined with general S-parameter simulations. Extensive circuit simulations of a proposed architecture unveil a variety of achievable designs of tunable BMAAs. Radar measurements of different implementations in the 77 GHz range and the theoretical analysis are in good agreement. The measurements show, inter alia, that the operational point of maximum biomimetically-increased phase sensitivity can be tuned over a range of 40° around the boresight direction, or that the power losses associated with BMAAs can be decreased by approximately 12 dB for weak radar targets, improving the detection capabilities.

INDEX TERMS Adaptive arrays, biologically-inspired antennas, biomimetic antenna arrays, direction-of-arrival estimation, millimeter-wave antenna arrays, tunable circuits, varactors.

I. INTRODUCTION

APART from the range and the velocity information, precise knowledge of the signal's DoA improves the perception of the environment with radar sensors [1], [2], [3]. The angle estimation accuracy depends on the antenna spacing in relation to the wavelength within an array and the signal-to-noise ratio [4]. The angular resolution, often defined using the Rayleigh criterion [5], also depends on the relative antenna spacing or the overall size of the aperture, respectively. Generally, a uniform linear array with an antenna spacing of one-half wavelength is a conventional trade-off between angular performance and grating lobes [6]. As the number of available channels is usually limited, a uniform element distribution might not be sufficient to fulfill the requirements of angular resolution, e.g., for automotive scenarios, even for Multiple-Input Multiple-Output (MIMO) radar setups [7]. Then, non-uniform, sparse arrays might be used, for which antenna elements are reconstructed with compressed sensing [8], [9]. Hence, the angular performance of radar sensors is strongly linked to the antenna spacing, as this is the most important variable that influences the measurable phase difference between the elements of an array.

Over the past decade, a bio-inspired approach was investigated by several research groups: the so-called Biomimetic Antenna Arrays (BMAAs). These arrays allow to shape the angular characteristic beyond the laws of conventional antenna arrays. Incorporating a Biomimetic Coupling Network (BCN) in between the antenna elements showed multiple benefits for different frequencies, technologies, and use-cases: First, the bio-inspired approach was proposed for arrays in the very high (VHF) and ultra high frequency (UHF) bands to improve direction-finding capabilities as antenna spacings of half-wavelength are often not feasible at those frequencies [10], [11], [12], [13]. As a consequence, the antenna elements are mutually coupled to a high degree,

which needs to be taken into account when designing the BCN. The same approach with high mutual coupling can be deployed at higher frequencies, as demonstrated at the infrared frequency of 28.3 THz [14]. Using a generalized model which is not dependent on mutual coupling [15], angular ambiguities of 1D [16] and 2D [17] MIMO arrays can be mitigated. Moreover, the Field of View (FOV) of unambiguous DoA estimation can be enlarged and an improvement of the angular separability is feasible [16]. For a monostatic on-chip MIMO array around 150 GHz the redundancy can be reduced and the virtual aperture enlarged [18]. It is also possible to design BMAAs with more than two antenna elements [19], [20], [21].

While a lot of benefits were demonstrated in the literature so far, most of the biomimetic coupling mechanisms were specifically designed for one measurement scenario with a fixed biomimetic characteristic. The BCN can only enhance the phase sensitivity of the array in a certain region of the DoA, either around the Boresight (BS) direction or at off-boresight (off-BS) angles [22]. Consequently, most BMAAs do not show any form of adaptivity depending on the target parameters. Exceptions of BMAAs with a form of tunability in the biomimetic coupling are [23] and [24]. In [23], one varactor diode is incorporated into a BMAA to mitigate the bandwidth limitations of electrically small antenna arrays. The resulting array can be operated between 580 MHz and 700 MHz. By integrating PIN diodes into a BMAA it is possible to switch between two operational modes [24]: a conventional array mode with better signal-to-noise ratio (SNR) and a biomimetic mode with enhanced phase sensitivity.

In this work, the concept of tunable BMAAs is introduced and multiple realizations with continuously changeable states are presented. The arrays with center frequency 76.5 GHz are based on the generalized model [15] and the antenna spacing is half-wavelength. The angular characteristics of a tunable BMAA can be adapted depending on the target's DoA and provide enhanced phase sensitivity for a broad angular range by controlling two varactor diodes in the BCN. The angle-dependent power loss associated with BMAAs is also tuned electronically and, thus, the proposed circuit also allows an adaptivity depending on the signal's SNR.

After a brief description of the fundamentals of BMAAs in Section II, Section III discusses the concept of a BMAA with tunable characteristic. This includes circuit requirements and design, and an overview of the design options that can be achieved. Radar measurements are conducted for four different realizations, as presented in Section IV. Finally, the measurement results are discussed in Section V.

II. FUNDAMENTALS

Conventional antenna arrays experience a phase difference between its antenna elements of

$$\phi_{\text{in}} = kd \sin\theta := 2\alpha \tag{1}$$

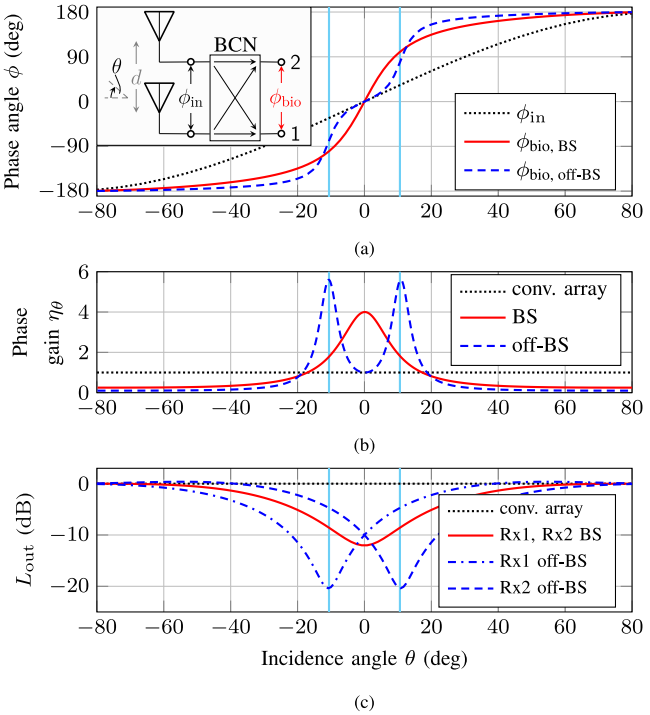

FIGURE 1. The three metrics of BMAAs for two distinct, exemplary BMAA configurations [24]. The BS BMAA (———) has its maximum phase sensitivity and output power loss at $\theta = 0°$. The off-BS BMAA (– – –) has its maximum effect at angles $\theta \neq 0°$, marked with vertical light-blue lines.

where k is the wavenumber, d the antenna spacing, and θ the angle of incidence of a plane wave. By biomimetically coupling two antenna elements with a BCN, see the inset of Fig. 1(a), the array characteristic is altered in both amplitude and phase. The three metrics to evaluate the behavior of such a BMAA are:

The Biomimetic Phase Difference ϕ_{bio}*:* BMAAs show a locally increased phase sensitivity indicated by a steeper course of the electrical phase difference for specific angles θ. Two examples of the biomimetic phase difference $\phi_{\text{bio}} = \angle u_2 - \angle u_1$ [25] between the two output ports in dependency of the angle of incidence θ are depicted in Fig. 1(a).

The Angle-Dependent Phase Gain η_θ*:* The angle-dependent phase gain [21], [24] expresses the slope of the biomimetic phase difference normalized to the differentiation of ϕ_{in}:

$$\eta_\theta(\theta) = \frac{\mathrm{d}\phi_{\text{bio}}(\theta)}{\mathrm{d}\theta} \Big/ \frac{\mathrm{d}\phi_{\text{in}}(\theta)}{\mathrm{d}\theta}. \tag{2}$$

Directions where $\eta_\theta > 1$ exhibit an increased phase sensitivity. The argument of its maximum reflects the angle of incidence where the biomimetic coupling has its maximum effect, cf. Fig. 1(b).

The Normalized Output Power Loss $\mathbf{L}_{\text{out}}$*:* Due to the biomimetic coupling, the output power of the antenna array is reduced in comparison to an equivalent, conventional array. The maximum reduction occurs at the angle of incidence

with the maximum increase in phase sensitivity. The corresponding metric is the normalized output power, depicted for two exemplary BMAAs in Fig. 1(c):

$$L_{\text{out}} = P_{\text{out,BMAA}} \Big/ P_{\text{out,conv. array}}. \tag{3}$$

Boresight (BS) BMAAs have their maximum steepness of ϕ_{bio} and thus the maximum phase gain $\eta_{\max} = \max(\eta_\theta)$ in the BS direction $\theta = 0°$. An off-boresight (off-BS) BMAA has its maximum phase sensitivity at two angles $\pm\theta \neq 0°$. Analogous, the maximum power loss $\min(L_{\text{out}})$ of the BS BMAA occurs at $\theta = 0°$, while the two ports of the off-BS BMAA have their minimum L_{out} at the off-boresight angles of maximum phase sensitivity. Their behavior is non-identical, though symmetric to $\theta = 0°$.

Generally, the output power of BMAAs is less than the output power of comparable conventional arrays ($L_{\text{out}} < 1$). A stronger increase in phase sensitivity corresponds to a larger maximum output power loss. While BMAAs have areas of enhanced phase sensitivity, their phase sensitivity is lower than the sensitivity of a conventional array for other angular regions. For BMAAs with maximum phase gain close to boresight, this is the case for angles approaching the end-fire direction ($\eta_\theta < 1|_{\theta\to\pm 90°}$), cf. Fig. 1(b).

III. CONCEPT

This section deals with the concept of a tunable BMAA. Thus, the goal is to construct a BMAA whose operational point, i.e., the angle of maximum phase sensitivity $\theta_{\eta_{\max}} = \arg\max \eta_\theta$, can be tuned electronically. First, the requirements for the desired task are discussed for a generally valid circuit representation of the BCN. Thereafter, the design process and the possible degrees of freedom in design are discussed for an exemplary circuit representation. By analyzing this exemplary circuit, physically reasonable simulation results are presented. However, the design methodology and the system configurations can be applied and defined for any circuit architecture.

A. REQUIREMENTS

In the following, a circuit-based simulation with S-parameters of the BCN is presented. In contrast to a model-based approach [22], this is a straight-forward method for the determination of the requirements of the BCN and the search of possibly suitable components to fulfill the desired task.

According to the schematic of a BMAA depicted in Fig. 2(a), the BCN is modeled as symmetrical two-port with S-parameters S_{BCN} and ideal connections to the antenna elements and the RF output ports. The element spacing is $d = \lambda/2$. For the chosen implementation of the antenna elements, the mutual coupling between the elements, and consequently the cross-admittance Y_{12}, are assumed to be negligible, see Section IV. Hence, one antenna element consists of an ideal current source with current $i_1(\omega,\theta) = A_0 e^{j\alpha}$ or $i_2(\omega,\theta) = A_0 e^{-j\alpha}$, respectively, and its self-admittance Y_{11}. $A_0 = 1$ is set without loss of generality. In the case of non-negligible mutual coupling, a parallel voltage-controlled current source should be added to the circuit representation of every antenna element [15]. The BMAA characteristic is represented by the maximum phase

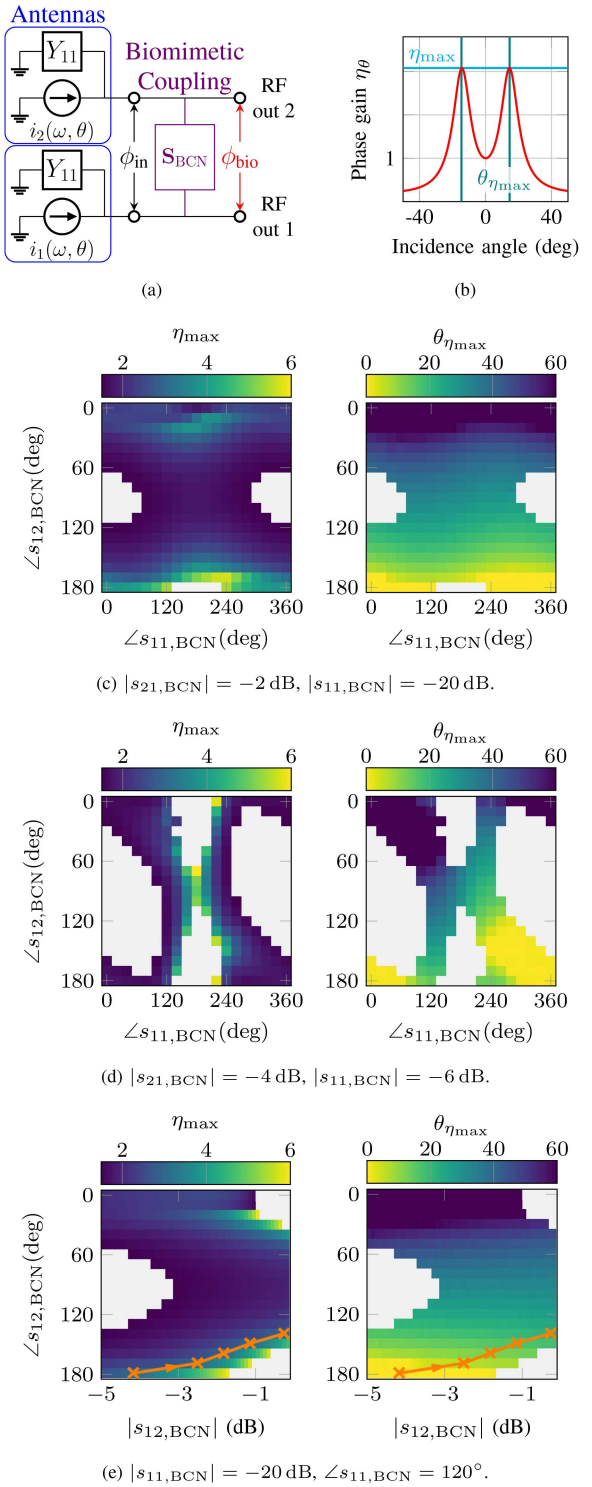

FIGURE 2. Schematic with BCN two-port (a) and definitions of the maximum phase gain $\eta_{\max}$ and the angle of maximum phase gain $\theta_{\eta_{\max}}$ (b). $\eta_{\max}$ and $\theta_{\eta_{\max}}$ for variations of the phases of S_{BCN} for fixed amplitude values (c), (d). $\eta_{\max}$ and $\theta_{\eta_{\max}}$ for a variation of $s_{12,\text{BCN}}$ for fixed values of $s_{11,\text{BCN}}$ (e).

TABLE 1. Exemplary BCNs for the tunability of $\theta_{\eta\max}$ with a variation of $\eta_{\max}$ versus with constant $\eta_{\max}$ in Fig. 2.

(a) $\theta_{\eta_{\max}}$ and $\eta_{\max}$ for $\angle s_{11,\mathrm{BCN}} = 120°$ in Fig. 2(c).

$\angle s_{12,\mathrm{BCN}}$	180	170	160	150	140
$\theta_{\eta_{\max}}$	0°	7°	12°	16°	19°
$\eta_{\max}$	5.6	3.5	2.9	2.4	2.1

(b) Required $s_{12,\mathrm{BCN}}$ for $\eta_{\max} = 3 = \mathrm{const.}$ in Fig. 2(e).

$\angle s_{12,\mathrm{BCN}}$	180	170	160	150	140
$\lvert s_{12,\mathrm{BCN}}\rvert$	-4.2	-2.6	-1.8	-1.1	-0.3
$\theta_{\eta_{\max}}$	0°	6°	12°	17°	21°

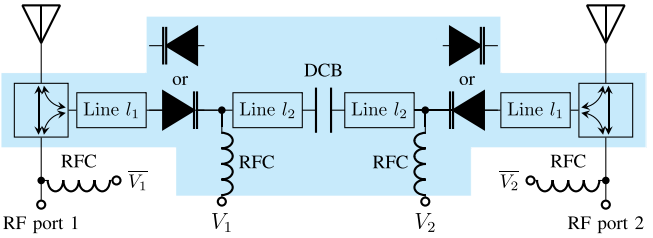

FIGURE 3. Schematic of the tunable BMAA. The BCN, highlighted in blue, is symmetrical with a DCB capacitor allowing independent biasing of the two varactor diodes. The symmetrically placed lines l_1 and l_2 are critical parameters to adjust the S-parameters of the BCN chain for a desired BMAA characteristic.

gain $\eta_{\max}$ and the angle of maximum phase sensitivity $\theta_{\eta_{\max}}$, see Fig. 2(b). To reduce the degrees of freedom of the circuit analysis, the amplitudes of S_{BCN} are set to fixed values: firstly, one state of strong transmission and good matching ($|s_{21,\mathrm{BCN}}| = -2\,\mathrm{dB}$, $|s_{11,\mathrm{BCN}}| = -20\,\mathrm{dB}$) and, secondly, one state where the transmission is reduced and higher reflections occur ($|s_{21,\mathrm{BCN}}| = -4\,\mathrm{dB}$, $|s_{11,\mathrm{BCN}}| = -6\,\mathrm{dB}$). Then, continuous sweeps of the phase values of S_{BCN} are performed. The sweep data extracted from the circuit simulation is further processed in a mathematical computing environment. The results are only depicted for a range of $1.5 < \eta_{\max} < 6$ (cf. Figs. 2(c) and 2(d)). This limits the analysis to configurations with a measurable increase in phase sensitivity, but reasonable power losses. Data points not complying with this condition are colored white. As the behavior is symmetrical around $\angle s_{12,\mathrm{BCN}} = 180°$, only the range of $0° \ldots 180°$ is depicted.

In the state of high transmission, see Fig. 2(c), the highest values of $\eta_{\max}$ are reached for a transmission phase of $\angle s_{12,\mathrm{BCN}} = 180°$. The reflection phase $\angle s_{11,\mathrm{BCN}}$ has less impact, due to the small reflection coefficient in this state, but influences the maximum phase gain that can be yielded nevertheless. The dependency between the operational angle $\theta_{\eta_{\max}}$ and $\angle s_{12,\mathrm{BCN}}$ is of particular interest: for $\angle s_{12,\mathrm{BCN}} = 180°$ the maximum phase gain is present at an angle of $\theta_{\eta_{\max}} = 0°$. For deviations from this phase of $s_{12,\mathrm{BCN}}$, the operational point of the BMAA is shifted to angles away from boresight. Thus, $\angle s_{12,\mathrm{BCN}}$ is the key parameter for the desired task of a tunable BMAA.

In case of higher reflections as in Fig. 2(d), the BMAA behavior is less predictable, because of the superposition of the reflected power fractions and the signal path transmitted through the BCN. Less combinations of $\angle s_{12,\mathrm{BCN}}$ and $\angle s_{11,\mathrm{BCN}}$ yield a BMAA behavior within the range of $\eta_{\max}$ specified above. Still in this case, the angle $\angle s_{12,\mathrm{BCN}}$ is the most effectual quantity to control the point of operation $\theta_{\eta_{\max}}$ of the BMAA.

For fixed transmission and reflection magnitudes of the BCN, the tunability of $\theta_{\eta_{\max}}$ away from the boresight direction is linked to a change of $\eta_{\max}$. Table 1(a) shows that a variation of $\angle s_{12,\mathrm{BCN}}$ for an exemplary value of $\angle s_{11,\mathrm{BCN}} = 120°$ in Fig. 2(c) results in the desired increase of $\theta_{\eta_{\max}}$, but also leads to a decrease of $\eta_{\max}$. Fig. 2(e) depicts a variation of the transmission values for the well-matched state of $|s_{11,\mathrm{BCN}}| = -20\,\mathrm{dB}$ and the same phase value of $\angle s_{11,\mathrm{BCN}} = 120°$. A decrease of $\eta_{\max}$ is visible for either a reduction of the transmission phase or a reduction of the transmission magnitude. The orange line in Fig. 2(e) marks the required values of $s_{12,\mathrm{BCN}}$ to tune $\theta_{\eta_{\max}}$ while keeping $\eta_{\max}$ at a constant value of 3. The specific values are listed in Table 1(b). It is evident, that for a constant strength of the biomimetic effect, it is necessary to control both phase and amplitude of $s_{12,\mathrm{BCN}}$ simultaneously. For non-negligible values of $s_{11,\mathrm{BCN}}$, all four parameters have to be set precisely in order to control $\theta_{\eta_{\max}}$ and $\eta_{\max}$ concurrently. In reality, such a high degree of control over the BCN values is not feasible. The most crucial requirements to ensure a controllable operation of the tunable BMAA are: low insertion losses of the overall BCN (and with it all integrated circuit components) to achieve the phase enhancement effect and little reflections for a good predictability of the BMAA behavior. To show the functionality of an adaptable $\theta_{\eta_{\max}}$, it is sufficient to focus on the capabilities to shift the phase of the BCN transmission path.

B. CIRCUIT DESIGN

Varactor diodes are regarded most suitable for the realization of the desired functionality and the tunability of the transmission phase of the BCN, cf. Section III-A. Other phase shifting components like microelectromechanical systems (MEMS) and liquid crystal phase shifters are not widely available, hard to handle and manufacture, or require high voltages. Packaged analog and digital phase shifters are not yet available at the design frequency of 77 GHz, are very large in relation to the operational wavelength or suffer from too high insertion losses. In contrast, single varactor diodes are small in size and have comparably low insertion losses.

One possible circuit architecture, used for the subsequent implementation, is depicted in Fig. 3. Two varactor diodes are incorporated in the BCN, highlighted in blue, to achieve a symmetrical circuit and to increase the maximum realizable shift in phase. The varactor diodes are always biased in reverse direction and can be controlled independently. The diodes are DC-isolated from each other with a DC block (DCB) capacitor. Hence, the polarity of both diodes can be interchanged. RF chokes (RFCs) allow biasing without

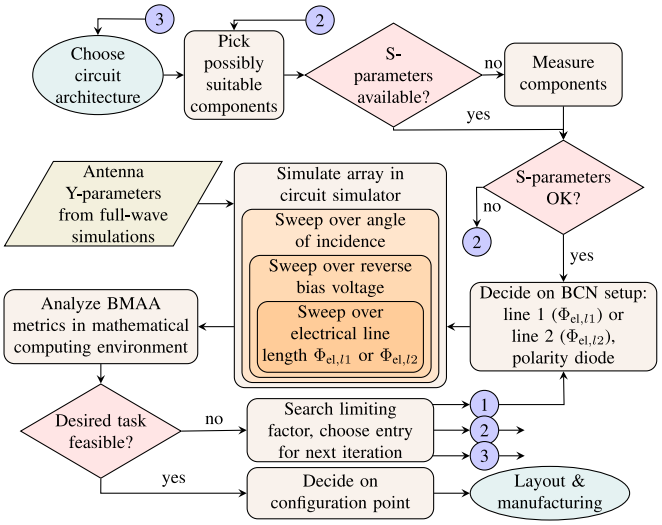

FIGURE 4. Design process of a tunable BMAA. The limiting factors for the achievable BMAA behavior are: the circuit architecture, the available phase shifting components, the implementation of the antenna elements, and the electrical line lengths $\Phi_{el,l1}$ or $\Phi_{el,l2}$.

TABLE 2. Characteristics of one varactor diode for simulations at 76.5 GHz (MACOM model MAVR-011020).

V_{rb}	$\angle \mathbf{s_{21}}$	$\lvert\mathbf{s_{21}}\rvert$	$\lvert\mathbf{s_{11}}\rvert$
0 V	−153°	−3.4 dB	−6.4 dB
⋮	⋮	⋮	⋮
9 V	⋮	⋮	−31 dB
22 V	−113°	−0.4 dB	−14 dB.

influencing the RF path. Antennas, RF ports, and the BCN are connected with each other by T-junctions.

By varying the reverse bias voltage over a varactor diode, its capacitance is altered, resulting in a change of its S-parameters in both amplitude and phase. To adjust the resulting transmission phase of the component chain forming the BCN to a specific biomimetic behavior, additional fixed line lengths are necessary. In the schematic in Fig. 3 those lines are either located directly between T-junctions and diodes (lines l_1) or in the center around the DCB (lines l_2).

The design process of the tunable BMAAs is shown in Fig. 4. First, a circuit architecture has to be chosen. Next, possibly eligible circuit components, here: biasing components and a varactor diode as phase shifting component, have to be selected. If the S-parameters are not provided by the manufacturer, the components have to characterized for which they are mounted on a printed circuit board (PCB). Precise phase information of the components is crucial, so contacting the circuit with microwave probes is preferred. The choice of the most suitable varactor diode is based on the achievable phase shift over the bias voltage range, minimal insertion loss, and good matching. In case of unsuitability of the chosen components, the characterization step has to be repeated for different components. Next, the circuit of Fig. 3 is simulated in a circuit simulator for a chosen polarity of the varactor diodes and the Y-parameters of the antenna elements, extracted from full-wave simulations of a two-element array. Simulation data is acquired for every angle of incidence, the measured range of the reverse bias voltage, and a variation of either line length l_1 or l_2. The simulation is further analyzed in a mathematical computing environment as explained in the subsequent Section III-C. If the desired functionality can be implemented, the array can be manufactured. Otherwise, adaptions have to be made and part of the design process has to be reiterated. The proposed re-entry points are marked with blue circles in Fig. 4 and are ordered in terms of additional design, characterization, and simulation time. Ideally, adaptions to the BCN setup are sufficient. Else, new circuit components have to be chosen and characterized or the circuit architecture has to be altered.

The design process is generally applicable for all implementations. Only the necessary design choices for the BCN setup may vary depending on the chosen component types and circuit architecture.

C. SYSTEM CONFIGURATIONS

In this section, all simulations relate to the schematic in Fig. 3, the components introduced in Section IV, and the tuning range of one varactor diode given in Table 2 in order to present simulations of physically feasible designs.

At first, the antenna array is simulated in a circuit simulator. The acquired data is exported to a mathematical computing environment. The quantities defining the BMAA behavior – the operational point $\theta_{\eta_{max}}$, the strength of the biomimetic effect η_{max}, and the minimum of L_{out} – are extracted from the simulated data of ϕ_{bio} and L_{out} for every line length and reverse bias voltage ($V_{rb} = V_1 = V_2$) $\leqslant 0$ V (depending on the chosen polarity of the varactor diodes). The obtained figures of merit are shown in Fig. 5 for a variation of either line 1 or line 2, cf. Section III-B. Figs. 5(a)−(c) show that the BMAA behavior changes quickly with a variation of the electrical line length of line 1 in the considered range $\Phi_{el,l1} = 20° \ldots 60°$. This fact emphasizes why precise knowledge of the S-parameters of the single components, in both amplitude and phase, is of particular importance for accurate simulation. While the BMAA experiences nearly no increase in phase sensitivity for $\Phi_{el,l1} = 20°$ and all reverse bias voltages, this setup yields to a phase gain of up to $\eta_{max} = 4.6$ for $\Phi_{el,l1} = 39°$ and $V_{rb} = 10$ V. The power losses range from 6.6 dB to 19.6 dB.

Additionally, the equivalent transmission phase of the BCN $\angle s_{12,BCN}$ is given in dependency of $\Phi_{el,l1}$ for 0 V and 22 V. The influence of the T-junctions is not included in the simulation of $\angle s_{12,BCN}$, but the T-junctions were designed to have little influence on the phase relations within the BMAA [21]. For 0 V, $\theta_{\eta_{max}}$ reaches 0° for $\Phi_{el,l1} < 36°$, because then $\angle s_{12,BCN}$ approaches 180°. For 22 V, $\angle s_{12,BCN} \approx 180°$ for an electrical length $\Phi_{el,l1} \approx 40°$. Thus, BS behavior ($\theta_{\eta_{max}} = 0°$) is expected for higher values

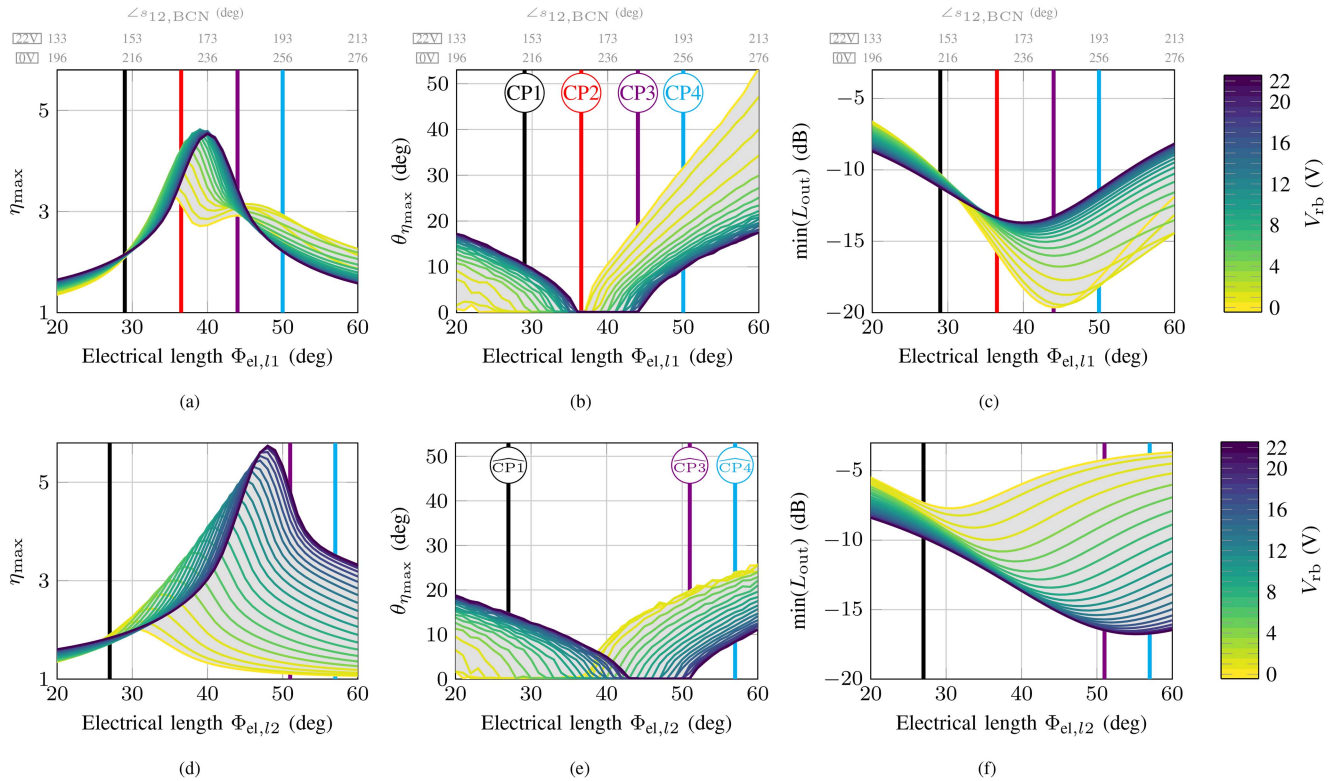

FIGURE 5. η_{max}, $\theta_{\eta max}$, and the minimum of L_{out} for a sweep of the electrical length of line 1 $\Phi_{el,l1}$ (a)–(c) or line 2 $\Phi_{el,l2}$ (d)–(f). Four line lengths of line 1 yielding a very different BMAA behavior over the reverse bias voltage are each marked as individual configuration point.

of $\Phi_{el,l1}$ for 22 V than for 0 V, matching with the simulations of Fig. 2.

Depending on the length of line 1, different BMAA characteristics can be reached for a variation of the bias voltage. Four configuration points (CPs) of clearly distinct behavior, representing possibly desirable array implementations, are marked in Fig. 5(b) and also highlighted in Figs. 5(a), (c).

(CP1) configuration point 1

The point of operation $\theta_{\eta max}$ is tunable, while the strength of the BMAA effect varies barely, meaning that η_{max} and $\min(L_{out})$ are very constant for a change of the bias voltage.

(CP2) configuration point 2

No change of the operational point $\theta_{\eta max}$ is present, but the strength of the BMAA effect is altered: only η_{max} and $\min(L_{out})$ vary over the reverse bias voltage V_{rb}.

(CP3) configuration point 3

An operation as BS BMAA and off-BS BMAA is possible with a maximum range of tunability of the angle of maximum phase sensitivity $\theta_{\eta max}$.

(CP4) configuration point 4

The operational angle $\theta_{\eta max}$ can be tuned, but the maximum phase sensitivity always occurs for angles off-boresight (no BS BMAA is feasible).

Both CP1 and CP3 show the possibility to reach a BS and an off-BS characteristic of the BMAA by varying the reverse bias voltage V_{rb}. In contrast to each other, the maximum $\theta_{\eta max}$ is reached for the maximum bias voltage (here: 22 V) for CP1, while the maximum $\theta_{\eta max}$ for CP3 is set for the minimal V_{rb}, here 0 V. For CP3 with an electrical line length of $\Phi_{el,l1} = 44°$, the phase sensitivity can be increased for targets in the range of $-19° < \theta < 19°$ with a phase gain of $\eta_{max} = 2.9 \ldots 3.5$ for this circuit setup. With power losses between 19.6 dB to 13.2 dB, it is apparent that the signal strength has to be strong enough to secure a detection of the target for all states of the array (all values of V_{rb}). Nevertheless, CP3 might be the most desirable configuration in measurement scenarios with a defined FOV of increased phase sensitivity around the BS direction. Otherwise, the tunability of the BMAA can also be provided by a configuration at CP1 ($\Phi_{el,l1} = 29°$) with less power losses (11.2 dB − 10.3 dB), but also a reduced range of $\theta_{\eta max}$ ($-11° < \theta < 11°$), and a reduced, but approximately constant, phase enhancement factor $\eta_{max} = 2.1$.

In Figs. 5(d)–(f) the same figures of merit are shown for an implementation of the BCN with line 2 instead of line 1 (cf. Fig. 3). For this setup, η_{max} can be as high as 5.7. The maximum power loss is less than 17 dB. For this setup, a BS BMAA with variable phase gain, see CP2 in Fig. 5(b), can not be defined over the whole

measured and simulated range of the reverse bias voltage V_{rb}. Particularly noteworthy for the setup in Figs. 5(d)−(f) is, that by lowering the bias voltage to $V_{\mathrm{rb}} = 0\,\mathrm{V}$, the maximum phase gain $\eta_{\max}$ is reduced to almost 1, corresponding to the phase characteristic of a conventional array. For $\Phi_{\mathrm{el},l2} = 51°$ ($\widehat{\mathrm{CP3}}$, corresponding to CP3 in Fig. 5(b)), a variation of $V_{\mathrm{rb}} = 22\,\mathrm{V} \rightarrow 0\,\mathrm{V}$ leads to a change of $\eta_{\max} = 4.8 \rightarrow 1.1$ and $\theta_{\eta_{\max}} = 0° \rightarrow 19.8°$. So while Fig. 5(e) indicates a tunability of the BMAA operational point, in fact, this setup corresponds to an array whose characteristic can be tuned between a BS BMAA with $\eta_{\max} = 4.8$ and a conventional array without enhanced phase sensitivity. For the state without phase enhancement (here: at $V_{\mathrm{rb}} = 0\,\mathrm{V}$) the power loss is only 4 dB.

IV. REALIZATION

One realization of a tunable BMAA is depicted in Fig. 6. The antenna elements are aperture coupled patch antennas with feed lines on the backside, bone-shaped apertures on the inner ground layer, and rectangular patches on the front of the PCB (design presented in [15], [21]). The PCB stack is built up by two 127 µm thick layers of Rogers RO3003 and a 3001 bonding film in between. Full-wave simulations of a two-element array provide the Y-Parameters: $Y_{11} = 17.48\,\mathrm{mS} + \mathrm{j}0.24\,\mathrm{mS}$ and $Y_{12} = 2.12\,\mathrm{mS} + \mathrm{j}4.41\,\mathrm{mS}$ [24]. As $\mathrm{Re}(Y_{11})$ exceeds $\mathrm{Re}(Y_{12})$ by one order of magnitude, we consider it reasonable to neglect the cross-admittance in the circuit analysis aligning with the simulations of previous works [21], [24]. The T-junctions [21], [26] and the intermediate circuit components form the BCN analog to the schematic in Fig. 3. The DCB is a 5.6 nF thin-film silicon capacitor from Murata and the RFCs are realized by two parallel quarter-wave transformed open-ended stubs [27]. The varactor diode used in all designs of this work is MAVR-011020 by MACOM. This diode has low losses, good matching, and a great phase shifting capability over the range of the bias voltage. The characterization results at the center frequency of 76.5 GHz correspond to the values of Table 2.

The specific circuit parameters used for the PCB designs of this work are listed in black in Table 3. Three layouts, Layouts 1a − 1c, are almost identical and only differ in the length of line 1. Even though the phase adjustment for Layouts 1a − 1c is realized with line 1, line 2 is non-zero for these setups, but implemented by a line length equivalent to an electrical phase shift of 180°. As line 2 is present twice in the BCN, these lines sum up to a transmission phase of 360° and do barely alter the BMAA behavior set by the length of line 1. The non-zero length of line 2 is necessary so that the RFCs have a sufficient spacing to each other. Additionally, one BMAA setup is fabricated where the phase adjustment of the BCN is solely realized by line 2 (Layout 2), corresponding to the simulations of Figs. 5(d)−(f). Again, an additional length equivalent to 180° is added to the desired line length.

TABLE 3. Realizations of two-element tunable BMAAs.

Layout	Line1 PCB (µm)	Line1 sim. (µm)	Line2 PCB (µm)	Line2 sim. (µm)	Diode polarity	cf. Config. Point
1a	362	312 (46°)	1242	1242 (180°)	⊣◀ ▶⊢	CP3
1b	307	257 (38°)	1242	1242 (180°)	⊣◀ ▶⊢	CP2
1c	253	203 (30°)	1242	1242 (180°)	⊣◀ ▶⊢	CP1
2	0	0 (0°)	1623	1573 (51°+180°)	▶⊢ ⊣◀	$\widehat{\mathrm{CP3}}$

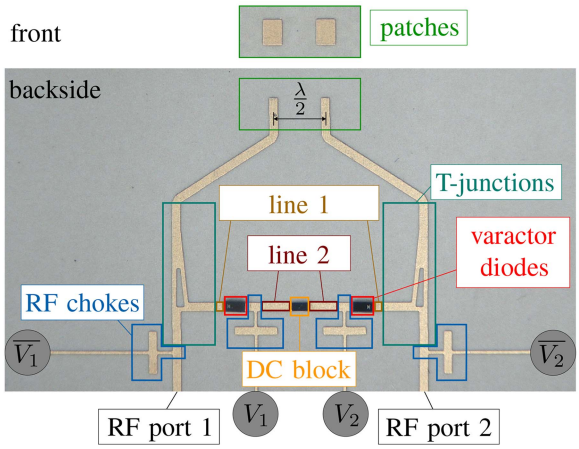

FIGURE 6. Photograph of a realized tunable two-element BMAA corresponding to Layout 1a of Table 3.

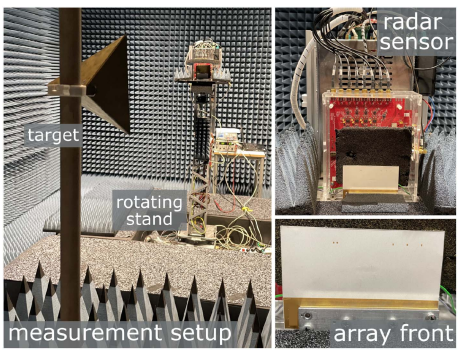

FIGURE 7. Measurement setup in an anechoic chamber. Array and radar sensor are connected with a waveguide transition, both being mounted on a rotating stand.

V. MEASUREMENTS

For validation of the circuit concept and its simulations, chirp-sequence radar measurements [28] with a bandwidth of 2 GHz are conducted in an anechoic chamber, see Fig. 7. The antenna array is connected to the radar sensor with waveguide transitions. Due to the choice of aperture coupled antenna elements, the feed network and the BCN are facing away from the target, a corner reflector placed in the BS direction of the array. Measurements are acquired for every bias voltage and turning angle of the rotating stand on which the radar sensor is mounted. After range-Doppler processing of the time-data [29], [30], the steering vector

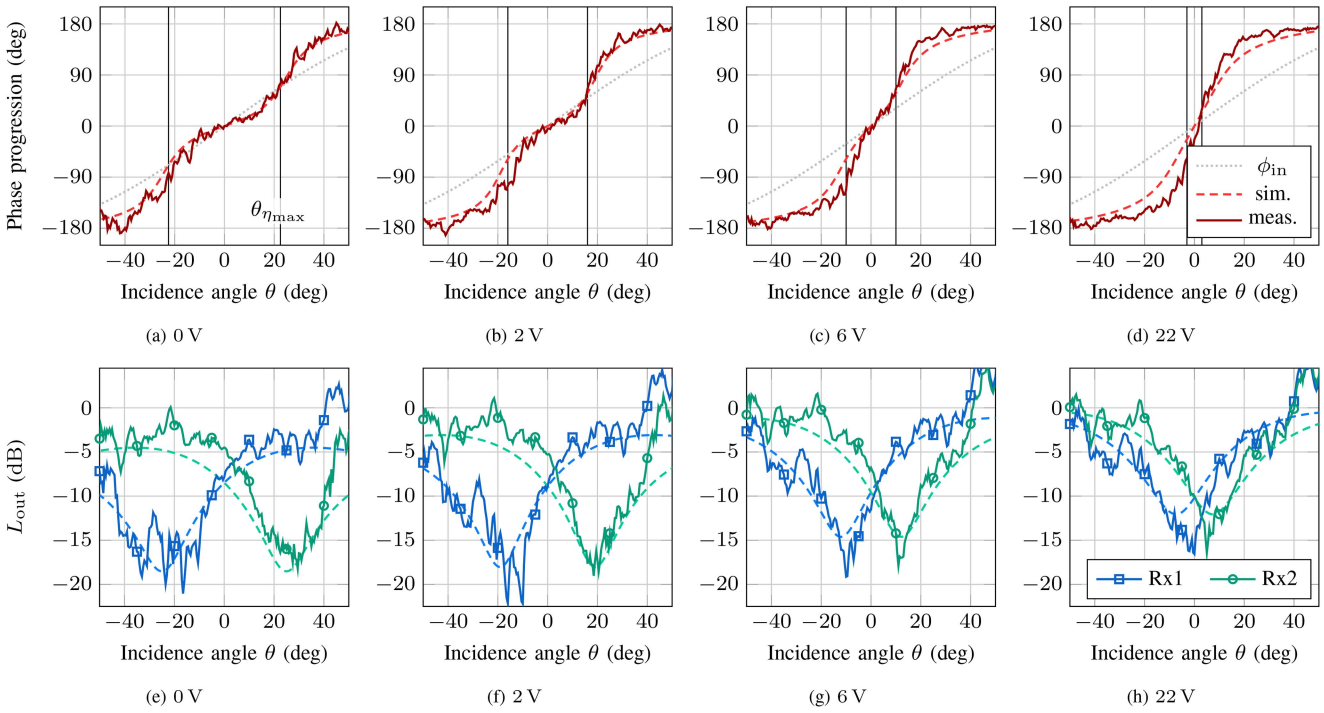

FIGURE 8. ϕ_{bio} measured for four different reverse bias voltages compared to the corresponding circuit simulation and the conventional phase progression ϕ_{in} for Layout 1a of Table 3 (8(a)−(d)). The angle of incidence of maximum phase sensitivity (marked with black vertical lines) shifts over the bias voltage. Measured (solid) and simulated (dashed) normalized output power L_{out} of the two array ports for the same bias voltages (e)−(h).

of the array-under-test is extracted from the target bin for every measurement [6].

Fig. 8 shows the measurement results for an array according to Layout 1a of Table 3 for four different bias voltages. The measurements are compared to circuit simulations of the same layout with real representations of the lines, instead of ideal lines as for the simulations in Fig. 5. The line length of line 1 is adapted in the simulation by a shift of $-50\,\mu\text{m} \approx -7°$ compared to the lengths on the PCB for good matching of simulations and measurements. This phase shift compensates for a cumulative error in the characterization measurements of the single components with microwave probes and is comparably small compared to the expected error for screwed PCB connections. The parameters used for the adapted simulations are listed in blue in Table 3. Additionally, the equivalent electrical length and the configuration point corresponding the layout best are given to facilitate a comparison with the simulations presented in Fig. 5. In Figs. 8(a)−(d) the measured ϕ_{bio} curves clearly show a BMAA behavior with enhanced phase sensitivity compared to the theoretical phase progression of $\phi_{\text{in}} = kd\sin\theta$. For $V_{\text{rb}} = 0\,\text{V}$, the maximum slope of ϕ_{bio} occurs at angles $\theta \approx \pm 23°$, corresponding to an off-BS BMAA behavior, while the maximum phase sensitivity approaches the BS direction for 22 V. Thus, the angle of maximum phase sensitivity $\theta_{\eta_{\max}}$ (marked with black vertical lines) is shifting with a change of the bias voltage as expected for this layout corresponding to CP3. For the corresponding measurements of L_{out} in Figs. 8(e) − (h), the incidence angles of maximum power loss $\arg\min(L_{\text{out}})$ match the positions of $\theta_{\eta_{\max}}$ and shift analogously over V_{rb}. The measured L_{out} of the two individual ports is very symmetric to the BS direction $\theta = 0°$. Due to increasing return losses of the varactor diode for $V_{\text{rb}} \to 0\,\text{V}$, L_{out} does not approach 0 dB for $|\theta| \to 50°$ anymore in both measurements and simulations. In general, measurements and circuit simulations agree to a very high degree.

Fig. 9 depicts the BMAA operational point $\theta_{\eta_{\max}}$ over V_{rb} for the three Layouts 1a−1c, which only differ in the length of line 1. The measured $\theta_{\eta_{\max}}$ values are extracted from a non-linear fit of the analytical BMAA equations for ϕ_{bio} and L_{out} [11], [18] to the measurement results. Fig. 9 shows that the tuning range of $\theta_{\eta_{\max}}$ varies significantly between the three Layouts 1a−1c, even though the only difference among the designs is a variation of the electrical line length of line 1 of $\Phi_{\text{el},l1} = 8°$. The direction of tunability differs between Layout 1a (maximum $\theta_{\eta_{\max}}$ for 0 V) and Layout 1c (maximum $\theta_{\eta_{\max}}$ for 22 V). For Layout 1b, the angle $\theta_{\eta_{\max}}$ is constant for most reverse bias voltages. The good match between simulations and measurements for all three layouts justifies the 50 µm shift applied to all simulations.

Fig. 10 shows the results for the array with Layout 2. The measurements confirm the simulated behavior corresponding to $\widehat{\text{CP3}}$ in Figs. 5(d)−(f): for 22 V the array features the characteristics of a BS BMAA, for 6 V ϕ_{bio} shows its maximum slope at an off-BS angle $\theta = 14°$, and at 0 V ϕ_{bio} is equivalent to the phase progression of a conventional array without a biomimetic coupling path. The minimum of

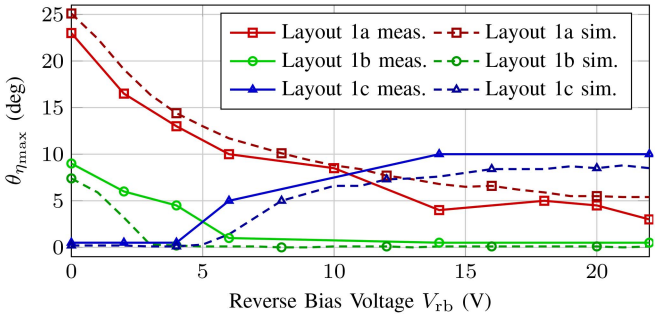

FIGURE 9. Incident angle of maximum phase sensitivity $\theta_{\eta\max}$ over the reverse bias voltage V_{rb} for three variations of Layout 1 showing a good match between simulations and measurements for all variations and different tuning ranges over the same voltage range.

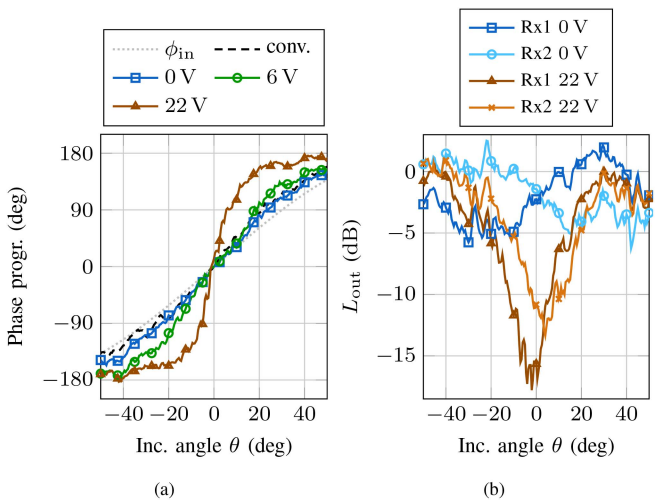

FIGURE 10. Measured phase progression and L_{out} for few reverse bias voltages for the array corresponding to Layout 2 in Table 3. The ϕ_{bio} curve for 0 V is equivalent to the phase progression of a conventional array.

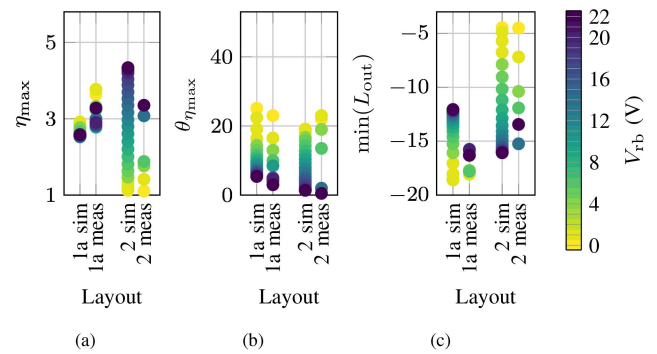

FIGURE 11. Simulated and measured BMAA figures of merit for Layout 1a and Layout 2 in dependency of the reverse bias voltage V_{rb}.

L_{out} (cf. Fig. 10(b)) at 0 V ranges from 0.5 dB to −5 dB. At 22 V, $\min(L_{\mathrm{out}})$ amounts to approx. −17 dB. Thus, the maximum power losses can be reduced by approximately 12 dB for radar targets with low SNR. L_{out} still shows an angular dependency in the mode of no phase enhancement ($V_{\mathrm{rb}} = 0$ V).

The simulated and measured figures of merit for the layouts presented in Figs. 8 and 10 are depicted in Fig. 11. This representation, corresponding to Fig. 5, highlights that despite Layout 1a and Layout 2 share a similar tuning range of $\theta_{\eta\max}$, Layout 2 exhibits a larger range of $\eta_{\max}$ and $\min(L_{\mathrm{out}})$. In contrast, Layout 1 has a clear increase in phase sensitivity over the whole tuning range of $\theta_{\eta\max}$ of $\eta_{\max} = 2.8 \ldots 3.8$ which comes at the price of maximum power losses between $\min(L_{\mathrm{out}}) = -18\,\mathrm{dB} \ldots -15.7\,\mathrm{dB}$.

VI. CONCLUSION

Tunable BMAAs with incorporated varactor diodes allow for a variety of different characteristica that overcome the physical law that only the antenna spacing can shape the phase sensitivity for angle estimation. The diverse designs can be useful for a multitude of scenarios and can be implemented without an exchange of the circuit components, but only by a variation of line lengths within the circuit. The tunability allows to match the BMAA operational range of enhanced phase sensitivity with the true target DoA for targets under any DoA around the tunable angular range. A multi-step operation of the tunable BMAA with biasing states of distinct angle-dependent power losses secures detection in at least one state (for weak radar targets). If the target is strong enough, the evaluation of the target information can be extended by setting the data of several BMAA states in relation to each other. Apart from the phase data, it is also conceivable to use the angle-dependent power loss as additional information for direction-of-arrival estimation in the future.

REFERENCES

[1] J. Fuchs, M. Gardill, M. Lübke, A. Dubey, and F. Lurz, "A machine learning perspective on automotive radar direction of arrival estimation," *IEEE Access*, vol. 10, pp. 6775–6797, Jan. 2022.

[2] I. Bilik, O. Longman, S. Villeval, and J. Tabrikian, "The rise of radar for autonomous vehicles: Signal processing solutions and future research directions," *IEEE Signal Process. Mag.*, vol. 36, no. 5, pp. 20–31, Sep. 2019.

[3] S. K. Joshi, S. V. Baumgartner, A. B. C. da Silva, and G. Krieger, "Direction-of-arrival angle and position estimation for extended targets using multichannel airborne radar data," *IEEE Geosci. Remote Sens. Lett.*, vol. 19, pp. 1–5, 2022.

[4] M. I. Skolnik, *Radar Handbook*, 2nd ed., M. I. Skolnik, Ed. New York, NY, USA: McGraw-Hill, 1990, p. 1.8.

[5] J. Hasch, E. Topak, R. Schnabel, T. Zwick, R. Weigel, and C. Waldschmidt, "Millimeter-wave technology for automotive radar sensors in the 77 GHz frequency band," *IEEE Trans. Microw. Theory Techn.*, vol. 60, no. 3, pp. 845–860, Mar. 2012.

[6] C. Vasanelli et al., "Calibration and direction-of-arrival estimation of millimeter-wave radars: A practical introduction," *IEEE Antennas Propag. Mag.*, vol. 62, no. 6, pp. 34–45, Dec. 2020.

[7] S. Sun, A. P. Petropulu, and H. V. Poor, "MIMO radar for advanced driver-assistance systems and autonomous driving: Advantages and challenges," *IEEE Signal Process. Mag.*, vol. 37, no. 4, pp. 98–117, Jul. 2020.

[8] C. M. Schmid, R. Feger, C. Wagner, and A. Stelzer, "Design of a linear non-uniform antenna array for a 77-GHz MIMO FMCW radar," in *Proc. IEEE MTT-S Int. Microw. Workshop Wireless Sens. Local Position. RFID*, Sep. 2009, pp. 1–4.

[9] F. Roos et al., "Compressed sensing based single snapshot DoA estimation for sparse MIMO radar arrays," in *Proc. 12th German Microw. Conf. (GeMiC)*, Mar. 2019, pp. 75–78.

[10] N. Behdad, M. A. Al-Joumayly, and M. Li, "Biologically inspired electrically small antenna arrays with enhanced directional sensitivity," *IEEE Antennas Wireless Propag. Lett.*, vol. 10, pp. 361–364, 2011.
[11] A. R. Masoumi, Y. Yusuf, and N. Behdad, "Biomimetic antenna arrays based on the directional hearing mechanism of the parasitoid fly ormia ochracea," *IEEE Trans. Antennas Propag.*, vol. 61, no. 5, pp. 2500–2510, May 2013.
[12] F. T. Dagefu, J. Oh, and K. Sarabandi, "A sub-wavelength RF source tracking system for GPS-denied environments," *IEEE Trans. Antennas Propag.*, vol. 61, no. 4, pp. 2252–2262, Apr. 2013.
[13] A. M. Elfrgani and R. G. Rojas, "Biomimetic antenna array using non-foster network to enhance directional sensitivity over broad frequency band," *IEEE Trans. Antennas Propag.*, vol. 64, no. 10, pp. 4297–4305, Oct. 2016.
[14] E. Mohammadi, B. Behzadnezhad, and N. Behdad, "An angle-sensing infrared detector using a two-element biomimetic antenna array," *IEEE Trans. Antennas Propag.*, vol. 66, no. 11, pp. 5818–5826, Nov. 2018.
[15] P. Grüner, T. Chaloun, and C. Waldschmidt, "A generalized model for two-element biomimetic antenna arrays," *IEEE Trans. Antennas Propag.*, vol. 67, no. 3, pp. 1630–1639, Mar. 2019.
[16] I. Dorsch, P. Grüner, M. Klose, D. Schmucker, and C. Waldschmidt, "Performance evaluation and optimization of MIMO radars using biomimetic antenna arrays," *IEEE Trans. Microw. Theory Techn.*, vol. 69, no. 11, pp. 5173–5184, Nov. 2021.
[17] P. Grüner, M. Klose, and C. Waldschmidt, "A radar system concept for 2D unambiguous angle estimation using widely spaced MMICs with antennas on-chip at 150 GHz," in *Proc. IEEE MTT-S Int. Microw. Symp. (IMS)*, Aug. 2020, pp. 1279–1282.
[18] P. Grüner, M. Geiger, and C. Waldschmidt, "Ultracompact monostatic MIMO radar with nonredundant aperture," *IEEE Trans. Microw. Theory Techn.*, vol. 68, no. 11, pp. 4805–4813, Nov. 2020.
[19] A. R. Masoumi and N. Behdad, "Architecture, design, and nonlinear optimization of three-element biomimetic antenna arrays," *IEEE Antennas Wireless Propag. Lett.*, vol. 12, pp. 1416–1419, Nov. 2013.
[20] M. R. Nikkhah, K. Ghaemi, and N. Behdad, "A three-element biomimetic antenna array with an electrically small triangular lattice," *IEEE Trans. Antennas Propag.*, vol. 65, no. 8, pp. 4007–4016, Aug. 2017.
[21] P. Grüner, I. Dorsch, and C. Waldschmidt, "N-element biomimetic antenna arrays," *IEEE Trans. Antennas Propag.*, vol. 69, no. 7, pp. 3899–3912, Jul. 2021.
[22] P. Grüner, S. Nguyen, T. Chaloun, and C. Waldschmidt, "Enhancing angle estimation for off-boresight targets using biomimetic antenna arrays," in *Proc. 48th Eur. Microw. Conf. (EuMC)*, Sep. 2018, pp. 1377–1380.
[23] M. R. Nikkhah, K. Ghaemi, and N. Behdad, "An electronically tunable biomimetic antenna array," *IEEE Trans. Antennas Propag.*, vol. 66, no. 3, pp. 1248–1257, Mar. 2018.
[24] I. Dorsch, D. Schwarz, and C. Waldschmidt, "A switchable biomimetic antenna array," *IEEE Antennas Wireless Propag. Lett.*, vol. 20, no. 12, pp. 2422–2426, Dec. 2021.
[25] A. R. Masoumi and N. Behdad, "An improved architecture for two-element biomimetic antenna arrays," *IEEE Trans. Antennas Propag.*, vol. 61, no. 12, pp. 6224–6228, Dec. 2013.
[26] G.-Y. Chen, J.-S. Sun, S.-Y. Huang, and Y. Chen, "The novel 3-way power dividers/combiners structure and design," in *Proc. IEEE Annu. Wireless Microw. Technol. Conf. (WAMICON)*, Dec. 2006, pp. 1–4.
[27] I. Flammia, T. Kleinfeld, M. Frei, A. Utreras-Rivera, and A. Stöhr, "71–76GHz grounded-coplanar-waveguide-to-rectangular-waveguide transition with integrated planar bias tee for quasi-hermetic radio-over-fiber wireless transmitter," in *Proc. 7th Eur. Microw. Integr. Circuit Conf.*, Oct. 2012, pp. 512–515.
[28] P. Hügler, F. Roos, M. Schartel, M. Geiger, and C. Waldschmidt, "Radar taking off: New capabilities for UAVs," *IEEE Microw. Mag.*, vol. 19, no. 7, pp. 43–53, Nov./Dec. 2018.
[29] V. Winkler, "Range doppler detection for automotive FMCW radars," in *Proc. 4th Eur. Radar Conf. (EuRAD)*, Oct. 2007, pp. 166–169.
[30] C. Schroeder and H. Rohling, "X-band FMCW radar system with variable chirp duration," in *Proc. IEEE Radar Conf.*, May 2010, pp. 1255–1259.

INES DORSCH (Graduate Student Member, IEEE) received the M.Sc. degree in electrical engineering from Ulm University, Ulm, Germany, in 2019, where she is currently pursuing the Ph.D. degree with the Institute of Microwave Engineering.

Her current research interests include biomimetic antenna systems in the microwave and millimeter-wave range and their applications in sensor networks.

Ms. Dorsch was a recipient of the Argus Science Award in 2019 and the IEEE Piergiorgio L. E. Uslenghi Letters Prize Paper Award in 2022.

DOMINIK SCHWARZ (Graduate Student Member, IEEE) received the M.Sc. degree from Ulm University, Ulm, Germany, in 2018, where he is currently pursuing the Ph.D. degree.

From 2011 to 2018, he was a student trainee with Hensoldt Sensors, Ulm. He joined the Institute of Microwave Engineering with Ulm University. His current research interests include automotive MIMO radars with a focus on high bandwidths, high channel counts, 2-D-DoA estimation, and novel multilayer PCB structures at millimeter-wave frequencies.

Mr. Schwarz was a recipient of the Ingenieure für Kommunikation Award in 2016 and the Argus Science Award in 2019.

SARAH FORSTER received the M.Sc. degree in electrical engineering from Ulm University, Ulm, Germany, in 2022.

She worked on biomimetic antenna systems with Ulm University. After graduating, she joined the Hensoldt Sensors GmbH, Ulm, as an RF Engineer. She is currently working on the development of high-frequency assemblies in the field of signal generation and reception for modern radar systems.

CHRISTIAN WALDSCHMIDT (Fellow, IEEE) received the Dipl.-Ing. (M.S.E.E.) and Dr.-Ing. (Ph.D.E.E.) degrees from the University of Karlsruhe, Karlsruhe, Germany, in 2001 and 2004, respectively.

From 2001 to 2004, he was a Research Assistant with the Institut für Höchstfrequenztechnik and Elektronik, University of Karlsruhe. Since 2004, he has been with Robert Bosch GmbH, in the business units Corporate Research and Chassis Systems. He was heading different research and development teams in microwave engineering, RF-sensing, and automotive radar. In 2013, he returned to academia. He was appointed as the Director of the Institute of Microwave Engineering, Ulm University, Ulm, Germany, as a Full Professor. He has authored or coauthored over 300 scientific publications and more than 25 patents. His research topics focus on radar and RF-sensing, mm-wave and submillimeter-wave engineering, antennas and antenna arrays, and RF and array signal processing.

Dr. Waldschmidt served as the Chair for the IEEE MTT-29 Technical Committee on Microwave Aerospace Systems and the MTT-27 Technical Committee on Wireless Enabled Automotive and Vehicular Applications. He was the TPC Chair and the General Chair of the IEEE MTT International Conference on Microwaves for Intelligent Mobility, for two times. In 2022, he was the General Chair of the German Microwave Conference. He was the Guest Editor of the *IEEE Microwave Magazine* and the IEEE MICROWAVE AND WIRELESS COMPONENTS LETTERS. Since 2018, he has been serving as an Associate Editor for IEEE MICROWAVE AND WIRELESS COMPONENTS LETTERS. He is a reviewer for multiple IEEE Transactions and many IEEE conferences in the field of microwaves and a member of the Executive Committee Board of the German MTT/AP Joint Chapter and the German Information Technology Society. Since 2020, he has been a member of the Heidelberg Academy of Sciences and Humanities.